nature materials

SUPPLEMENTARY INFORMATION

DOI: 10.1038/NMAT3403

Van derWaals interactions at metal/organic interfaces at the single-molecule level

I. Experimental details

Experimental Setup and Procedures:

We have modified a commercial AFM head (Veeco Multimode) with customized optics to maximize signal-to-noise ratio for our measurements. We use commercially available filters, adders (SRS), data acquisition instrumentation (National Instruments PXI) and current amplifier (Keithley 428). We use a calibrated single-axis piezoelectric positioner (Mad City Labs) which is driven by a high resolution 24-bit PXI-4461 card. A constant bias is applied between the Au coated mica substrate and the Au coated AFM tip (NanoAndMore USA) using the same card. The AFM cantilevers are coated with 35 nm of Cr and 120 nm of gold (99.9999% pure, from Alfa Aesar) through thermal evaporation. The substrates are mica sheets with 100 nm of evaporated gold (99.9999% pure, from Alfa Aesar). Before every experiment, we clean the cantilever and substrate in a UV/ozone cleaner.

Each simultaneous measurement of conductance and force begins by contacting the tip to a substrate to a conductance larger than $5G_0$. This ensures that we sample a wide variety of junction structures in our measurements. From this position, we pull the substrate away from the AFM tip at the rate of 18 nm/s and measure the current and force with an acquisition rate of 100 kHz. The positioner is calibrated by the manufacturer as well as independently by us using laser interference measurements to be accurate within 5%.

Force calibration:

We obtain force data by measuring the deflection of a focused laser beam off the back of the AFM cantilever. This beam is collected on a quadrant detector and the voltage signal is converted into a force reading in three steps:

1) We obtain the voltage signal during a 200 nm motion of the cantilever in hard contact with the substrate. Since we know the piezo displacement, we can calculate the conversion factor for the voltage signal to cantilever displacement.

2) We measure the power spectrum of the free cantilever displacement. Fitting the resonant peak to a Lorentzian profile allows us to extract the stiffness of the cantilever using established methods[1].

3) For each experimental dataset, we obtain the rupture force for clean gold samples, and perform a Gaussian fit to this data. The combined errors in the measurements of the voltage-to-displacement factor and cantilever stiffness as well as known variability in detector sensitivity[2] manifest themselves in the mean value of the Au-Au rupture force[3]. We have rigorously characterized this value by compiling more than 10,000 individual Au rupture events (out of 39,000 measurements performed with multiple tips, substrates and calibrations) using the same algorithm described in Section II. Figure S1 shows the histogram of these forces along with a Gaussian fit centered at 1.5 ± 0.02 nN (fitted mean ± standard error). With day-to-day changes in AFM tips, substrates and calibrations, we observe that the mean rupture force of Au G_0 (compiled from 1000-3000 measurements of clean Au before deposition of molecules) is Gaussian distributed, but the mean varies by up to a maximum of ±20% of 1.5 nN. Therefore, we correct for these day-to-day calibration errors across datasets by using a single correction factor per dataset, such that the mean Au G_0 rupture force is set to the reference value of 1.5 nN. The absence of this correction does not affect the observed trends, and its influence on the quantitative results is reduced due to averaging of multiple datasets.

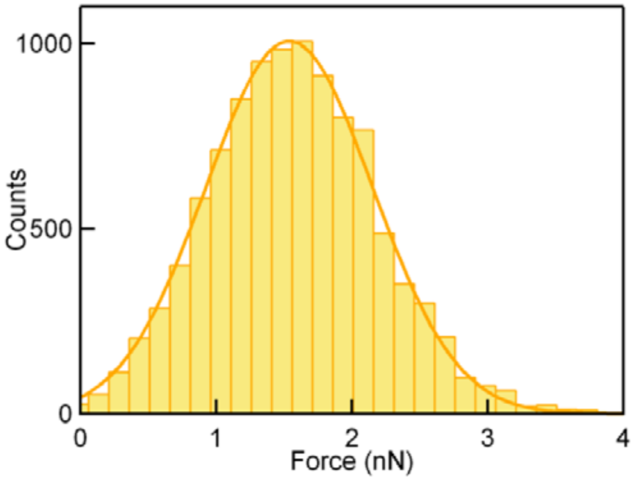

Figure S1. Histogram of Au G_0 rupture forces (compiled from more than 10,000 individual measurements) can be fitted to a Gaussian profile, and the most frequently measured value obtained is 1.5 nN.

DOI: 10.1038/NMAT3403

Results from Control Measurements:

We have carried out control measurements with 4-phenyl-pyridine (4PP) and 4-styryl pyridine (4SP) (obtained from Sigma Aldrich). These are analogous to the two molecules used in the manuscript, 4,4' bipyridine (BP) and 1,2-bis(4-pyridyl)ethylene (BPE) respectively, except that they have a pyridine group on only one end and a phenyl group on the other. The conductance measurements with these compounds did not show well-defined conductance plateaus and no clear peaks appear in the linear binned conductance histograms (Figure S2A). This demonstrates that no well-defined conducting junctions are formed with molecules that have only one pyridine link. Force measurements from the longer compound (4-styryl pyridine, 4SP) do not show any saw-tooth rupture events beyond the Au G_0 rupture. Using a force event detection algorithm as detailed in our previous work[4], the rupture force distribution in SI Figure S2B shows that a negligible fraction of traces have force events beyond the set threshold value of 0.3 nN (~2× standard deviation of instrument noise). If specific Au-C interaction were the sole reason for the observed large rupture force of BPE, their presence would be expected to result in a measurable rupture force for 4SP. Finally these control measurements with 4SP show that in this case, non-specific vdW interactions are not sufficient to form junctions with well-defined conductance plateaus or force events at room temperature.

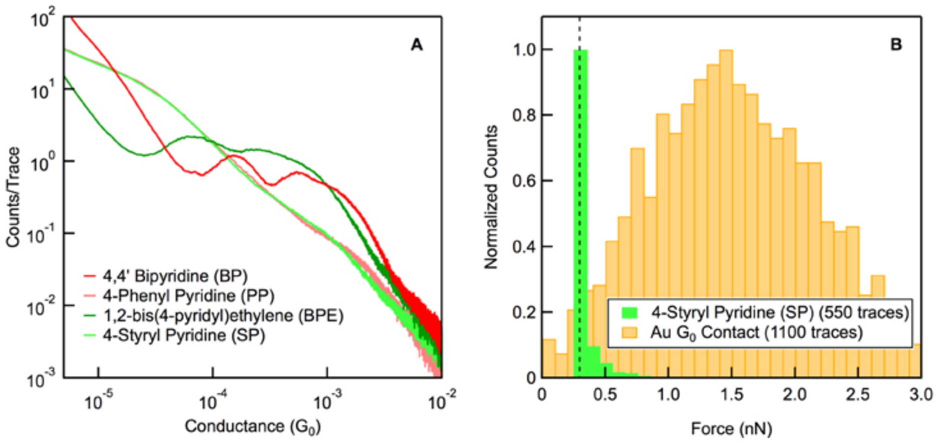

Figure S2. (A) Conductance histogram for BP, PP, BPE, and SP generated from over 6000 traces, using linear bins of width 10^{-6} G_0. (B) Histogram of forces measured in the presence of SP for the G_0 single atom contact (in yellow) and for the largest force event greater or equal to a preset threshold value of 0.3 nN (dashed line) measured beyond the G_0 contact rupture.

II. Data analysis

Algorithm:

We have developed an algorithm (Figure S3) to identify structural rearrangement signatures in the force data and use it to compile statistically relevant datasets of rupture force, stiffness and rearrangement lengths. We first start by finding the displacement position where the conductance plateau of interest ruptures to noise levels. This point is then used as a datum for further force analysis. All significant force events before this point are identified by a subroutine that locates *sharp and large* force fluctuations. This procedure consists of separately analyzing high and low pass filtered force data, and finding the locations at which sharp (large high frequency components) and large (large low frequency components) events occur coincidentally. Every force fluctuation above 0.25 nN, (~1.5× standard deviation of instrument noise) is identified in this manner. To be included in the results, we require that: a) the conductance beyond the plateau of interest drops to conductance noise levels to ensure that we are analyzing a junction rupture event, and b) the final load-rupture saw-tooth have at least 100 datapoints, to ensure meaningful fitting required in analyzing the stiffness. Each individual measurement satisfying these two criteria are included in the results and without any further selection. This ensures that there is no selection based on rupture force, stiffness or rearrangement length. The total number of traces represented in the final results (Figures 1-3 in the main text) are: Au G_0 – 2346 , BP_H – 4118, BP_L – 7763, BPE_H – 530, and BPE_L – 501.

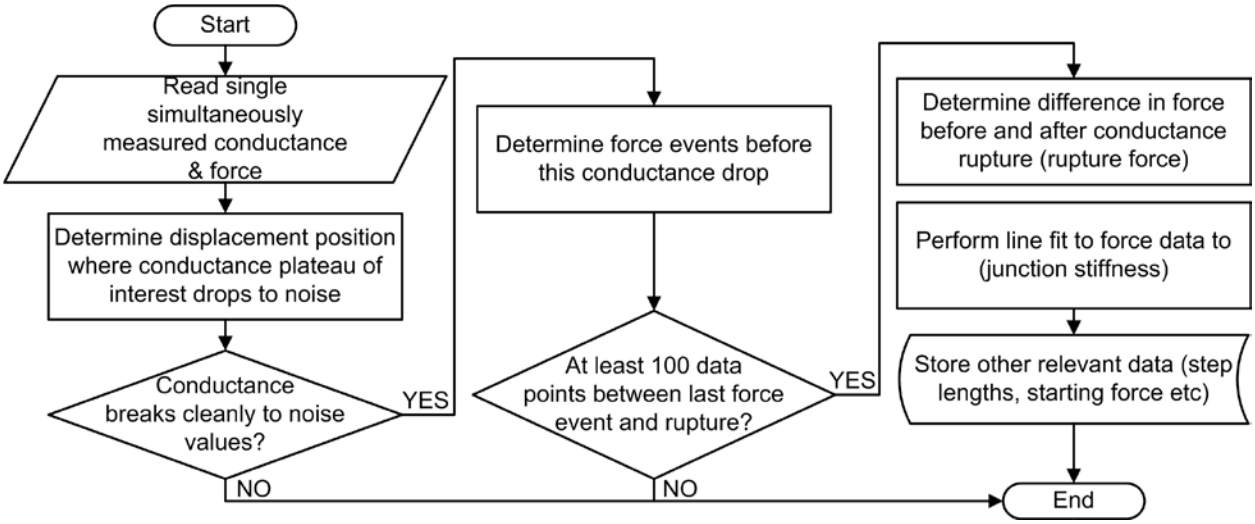

Figure S3. Flow chart explaining the algorithm to obtain rupture force and stiffness.

Analysis details:

Figure S4 demonstrates the algorithm for two traces with BP_H plateaus along with their intermediate structural rearrangements, as demonstrated by the force events during the nominal conductance step, that proceed to a ruptured junction after elongation. The green vertical lines show the locations where large force fluctuations are identified by the algorithm. The value of the force drop at the junction rupture location is the rupture force. The force data between the rupture location and the force event that immediately precedes the rupture is fitted with a linear fit to obtain the slope (k_{raw}) of the force ramp. The stiffness of the junction (k_{junc}) is then obtained after correcting for AFM spring constant (k_{cant} ~50 nN) in series: $k_{junc} = k_{raw} \cdot k_{cant} / (k_{cant} - k_{raw})$.

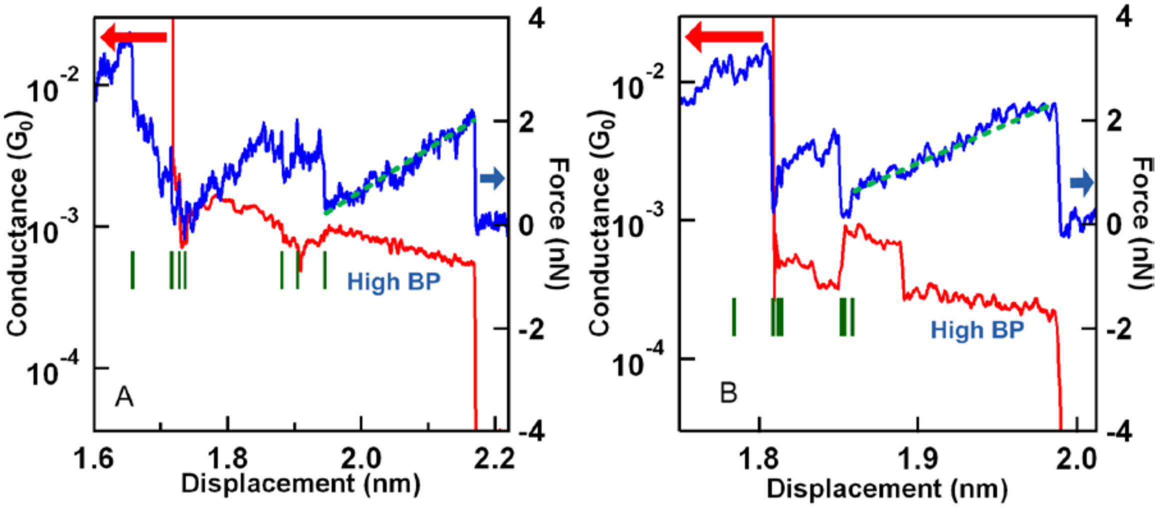

Figure S4. Two sample zoomed-in traces showing algorithmic recognition of BP_H rupture and rearrangement. Green vertical lines are identified force events and dotted lines are linear fits to the force ramp of the final loading event. Conductance fluctuations are sometimes, though not always, observed accompanying the force fluctuations.

In addition to junction rupture force, we can also obtain information about the force required to switch between the high and low conductance structures by a slight modification of the algorithm. For instance, in the case of BP_H switching to BP_L, we need to account for the initial loading on the BP_L structure. Due to this subtlety, we start with the traces where low BP_L breaks to noise levels (as described above) and then analyze these traces further to locate BP_H plateaus preceding the BP$_L$ plateaus. The breaking forces for the BP$_H$ structures in this case are referred to the absolute zero of the force beyond the BP$_L$ rupture (Figure S5). We therefore avoid underestimating the rupture force of the BP$_H$ structures. The difference in the rupture forces of the high and low conductance junction characterizes the switching force required to induce the structural transition.

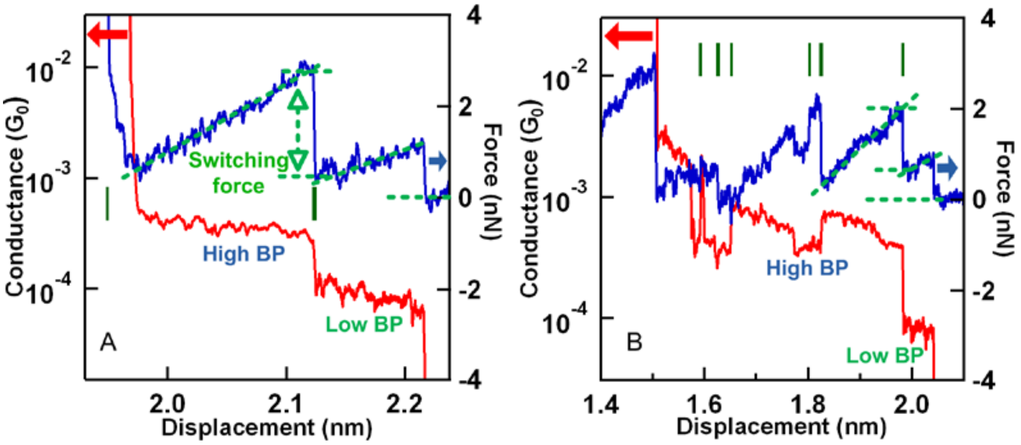

Figure S5. Two sample zoomed-in traces showing algorithmic identification of high to low switching in BP junctions. Higher stiffness of BP$_H$ junctions is clearly seen. For traces with high-to-low switching, BP$_H$ rupture force is referred to the absolute zero beyond BP$_L$ rupture and the difference in force between the breaking of BP$_H$ and formation of BP$_L$ is the switching force. Green vertical lines are identified force events and dotted lines represent junction stiffness of the final structures.

Table ST1 summarizes the mean values of measured forces and stiffness for Au G$_0$, BP$_H$ and BP$_L$ junctions, including BP$_H$-BP$_L$ switching. The non-zero switching force implies that the high and low conductance structures are indeed significantly different, and that the switching between these two states involves an abrupt structural change. We note that the relatively large starting forces indicate that, on average, the junctions form under a non-zero tensile stress. We also observe that there is only slight difference in rupture force and stiffness between those BP$_H$ junctions that rupture and those that switch to the low conductance state, indicating that their binding is not significantly different.

Table ST1. Summary of forces and stiffness of various Au and BP junction evolution scenarios.

Scenario	Rupture Force (nN)	Junction Stiffness (N/m)	Starting Force (nN)	Switching Force (nN)
Au G_0–rupture	1.50 ± 0.01	7.7 ± 0.3	1.07 ± 0.01	
BP_H–rupture	1.48 ± 0.01	10.2 ± 0.2	0.73 ± 0.01	
BP_L–rupture	0.85 ± 0.01	6.7 ± 0.1	0.52 ± 0.01	
BP_H–switch–BP_L	1.31 ± 0.02	9.3 ± 0.2		0.60 ± 0.02

III. Theoretical calculations

DFT methods:

To estimate the role of dispersion interactions in the bond rupture process, the semi-empirical Grimme DFT-D2 approach[5] implemented in VASP has been employed. Several estimates for the C6 coefficient for Au appear in the literature[6-8] ranging from 220 to 615 eV- Å^6. We use C6 = 422 eV-Å^6 with R0 = 1.772 Å. The additional Au-Au interaction is relatively strong. As noted in the context of the recently revised Tkatchenko-Scheffler semiempirical scheme, the effect of screening is important in the metal[9]. In the DFT-D2 approach, we limit the range of the d^-6 interactions with a relatively short cut-off (6 Å). The bulk fcc lattice parameter for Au is calculated to be 4.13 Å with these parameters in the DFT-D2 scheme, about 1% larger than experiment. The generalized gradient approximation (PBE) gives 4.17 Å, indicative of the extra attractive interaction in the DFT-D2 scheme. The periodic slabs in the supercell geometry employed assure more than 10 Å separation between the tip of the molecule and the first layer of Au in the next cell above. The lateral cells employed (4x5 and 5x5) for the bipyridine studies assure that the interaction between the additional dipole associated to the N-Au donor-acceptor bond in the primary cell and those in the periodic replicas contribute less than 0.05 eV to the binding energy. This conservative estimate is based on our prior analysis of ammonia bonding to an Au adatom[10] and 1/d^-3 scaling. Finally, the use of a 3 ML Au slab is consistent with the relatively short cut-off used in the DFT-D2 approach. Further, single point calculations indicate that an additional Au layer has a minimal impact on the binding energy (<0.05 eV).

For calibration, we considered the adsorption energy of benzene flat on the Au(111) surface. We found a relatively reasonable adsorption energy, 0.88 eV, with the benzene at 3.0 Å above the plane of the surface. These results are close to those reported for benzene on Ag(111) (0.81 eV and 2.93 Å) using the new Tkatchenko-Scheffler scheme. Application of an approach based on the van der Waals Density Functional approach[11] gave weaker binding (0.42 eV and 3.7 Å)[12]. A desorption energy of 0.64 eV has been estimated from temperature programmed desorption (TPD) experiments[13]. There is some evidence that the standard choice of prefactor (1×10^{13} s^{-1}) is too small for larger molecules[9, 14]. With values as high as 1×10^{18} s^{-1}, the estimated desorption energy could be as large as 0.88 eV. This test suggests that the DFT-D2 approach overestimates van der Waals interactions involving Au for this parameter set. For a single ring, the error could be as much as 0.24 eV, depending on the interpretation of the TPD experiments.

Results:

Our previously published calculations of adiabatic trajectories for 4,4'-bipyridine were based on pyramidal cluster models for the tips (20 Au atoms for each tip) and designed to simulate the low conductance configuration in the experiments; dispersion interactions were not considered[15]. When focusing on a single link bond to the apex of a symmetric pyramid and with the backbone of the BP oriented vertically, a maximum sustained force of 1.11 nN was calculated (Table ST2). Here we perform similar calculations with a slab model plus a small pyramidal tip (4 atom) in a 4×5 surface unit cell. These trajectories are calculated with steps of 0.1 Å or 0.2 Å and structure relaxation to a force criterion of 0.03 eV/Å at each step. The backbone is initially tilted about 20 degrees from normal and a similar force results (Table ST2). For a single adatom tip, the binding energy is larger and the maximum sustained force increases to 1.5 nN (Figure S6). Interestingly, for this modest backbone tilt angle, there is a step in the trajectory where the adatom jumps to an adjacent hollow site. This illustrates that details of the Au atomic structure near the link bond point affect binding energy and hence maximum sustained force, as one would expect on general grounds. When the dispersion interaction is included as a perturbative correction using the structure optimized with PBE only, the maximum sustained force increases slightly (0.14 nN and 0.18 nN for the 4 atom pyramid and the adatom respectively). As a comparison, a trajectory for the adatom tip was also computed with the dispersion interaction included in the geometry optimization. The binding energy and maximum force are very similar, although the adatom does not shift due to its stronger adhesion to the surface within the Grimme scheme.

Table ST2. Comparison of binding energy and maximum sustained force for a series of link-electrode structures and computational approaches.

Configuration / Theory	Binding Energy (eV)	Maximum Force (nN)
Pyramid model / PBE	0.75	1.11
Slab + 4 atom tip / PBE	0.81	1.12
Slab + adatom tip / PBE	0.97	1.5
Slab + 4 atom tip / PBE + vdW (geo PBE)	0.96	1.26
Slab + adatom tip / PBE + vdW (geo PBE)	1.16	1.68
Slab + adatom tip / PBE + vdW (geo PBE+vdW)	1.14	1.69

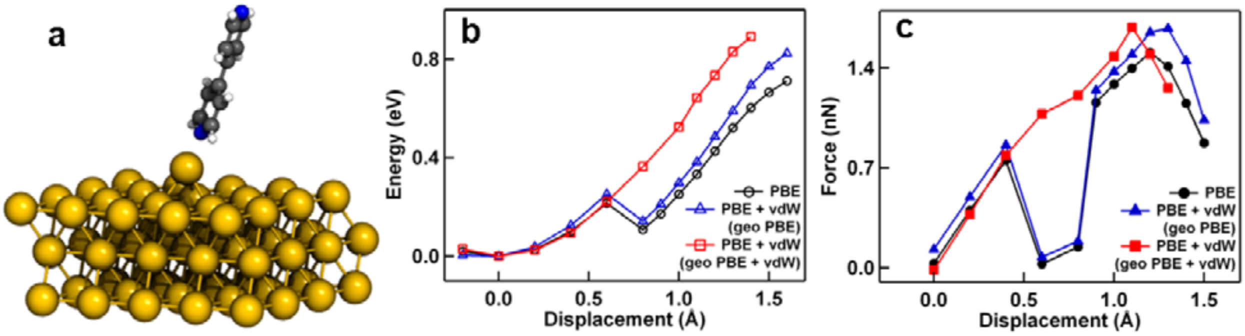

Figure S6. (a) Relaxed structure near minimum energy for the adatom tip model. Energy (b) and force (b) versus elongation (zero taken from the minimum energy point) with three approximations: PBE, PBE + vdW (geometry optimization with PBE), and PBE+vdW (geometry optimization with PBE including vdW forces).

Taken together, these calculations show that the binding to an isolated tip structure supports a range of maximum sustained force that is in good overall agreement with the range of the histogram of measured rupture forces for breaking from the BP_L structure and that in the BP_L structure the influence of van der Waals interaction is small.

When the dispersion forces are included in the geometry optimization, we find that the adatom is more than 0.1 Å closer to the surface, indicative of stronger binding to the surface. For larger superstructures (pyramidal or ridge), inclusion of the dispersion forces causes substantial distortion. The C6 coefficient for an individual Au atom is large. However, within a metallic structure, the vdW interaction should be screened. We therefore believe that the distortions of these superstructures are exaggerated in the DFT-D2 scheme. We have shown in Table ST2 that for the adatom link case inclusion of the dispersion forces as compared to the perturbative approach where the vdW energy is added as a correction based on the structure determined in PBE gives very similar results for the binding energy and maximum sustained force. In the junctions under study here, there is a significant, specific chemical interaction between the N atom in the pyridine ring and the Au atom on the electrode. For most of the trajectory under study, this substantially controls the geometry. This contrasts with the case of benzene flat on the surface where the dispersion interaction has a substantial impact on the equilibrium distance above the surface. Only late in the trajectory when the N-Au bond is breaking and the Au link atom is retracting towards the surface, then the dispersion attraction may affect the geometry in a way that would slow down the loss of binding energy and hence the force trajectory.

To illustrate the force induced by the dispersion attraction between the pyridine ring and the edge of an asperity, we consider a simplified example in Figure S7. A benzene molecule starts flat on a Au(111) facet at the minimum energy distance from the surface, but near the edge of the facet (to another, equivalent facet). The benzene molecule is pulled along a straight line at a uniform rate across the edge of the facet. The dispersion energy and force are calculated from the Grimme model with the parameter set used here, but there is no atomic relaxation allowed. As can be seen in the force trajectory in Figure S7, as the back of back portion of the molecule passes the edge, the force goes through a maximum, the magnitude of which is about 0.4 nN. In a realistic junction where there are specific chemical interaction involved, the local rate at which the ring passes the asperity can be faster than the average. For the portion of the trajectory in Figure 4f in the text where the force is going through its maximum value, the specific N-Au bond is breaking and the increment to that bond length is larger than the average step in the trajectory, determined by the portion of the junction that is held by constraints. The sustained force is determined by the change in energy (largely driven by local changes in structure near the bond), divided by the change in separation between the constraints (the average step of the trajectory). Thus, the 0.4 nN dispersion contribution to the maximum force found for a uniform rate (Figure

S7) is likely a lower bound while the 1 nN determined from the PBE trajectory in Figure 4e,f, without the potentially moderating influence of the dispersion forces, is likely an upper bound.

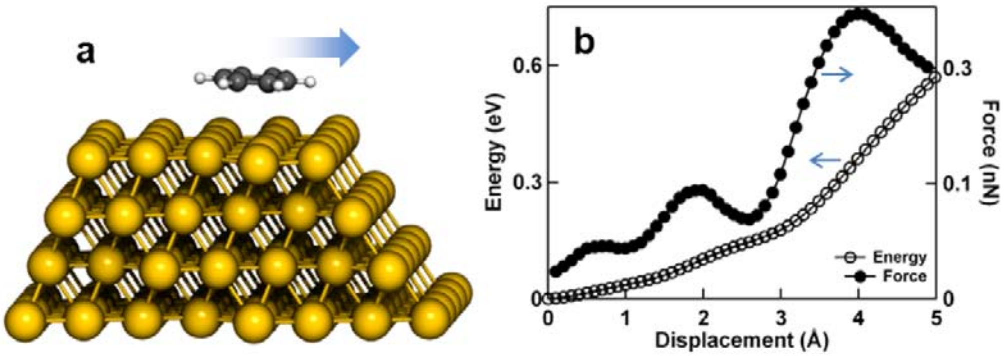

Figure S7. Model structure (a) and corresponding energy and force (b) versus displacement when the benzene is pulled straight across the facet edge, resulting in a reduction in the dispersion interaction.

Finally, several different structures were explored to look for evidence of specific bonding interactions between C atoms in the pyridine rings and undercoordinated Au structures. No examples were identified in which either a significant extra binding energy, beyond dispersion interactions, or a distortion of the ring indicative of C-Au bond formation was seen.

IV. References

(1) Hutter, J. L.; Bechhoefer, J. *Rev. Sci. Instrum.,* **1993,** 64, (7), 1868-1873.
(2) Huisstede, J. H. G.; van Rooijen, B. D.; van der Werf, K. O.; Bennink, M. L.; Subramaniam, V. *Opt. Lett.,* **2006,** 31, (5), 610-612.
(3) Rubio-Bollinger, G.; Bahn, S.; Agraït, N.; Jacobsen, K.; Vieira, S. *Phys. Rev. Lett.,* **2001,** 87, (2), 026101.
(4) Aradhya, S. V.; Meisner, J. S.; Krikorian, M.; Ahn, S.; Parameswaran, R.; Steigerwald, M. L.; Nuckolls, C.; Venkataraman, L. *Nano Lett.,* **2012,** 12, (3), 1643-7.
(5) Grimme, S. *J. Comput. Chem.,* **2006,** 27, (15), 1787-1799.
(6) Sławińska, J.; Dabrowski, P.; Zasada, I. *Phys Rev B,* **2011,** 83, (24), 245429.
(7) Tonigold, K.; Gross, A. *J. Chem. Phys.,* **2010,** 132, (22), 224701.
(8) Toyoda, K.; Hamada, I.; Lee, K.; Yanagisawa, S.; Morikawa, Y. *J. Chem. Phys.,* **2010,** 132, (13).
(9) Ruiz, V. G.; Liu, W.; Zojer, E.; Scheffler, M.; Tkatchenko, A. *Phys. Rev. Lett.,* **2012,** 108, (14), 146103.
(10) Hybertsen, M. S.; Venkataraman, L.; Klare, J. E.; Whalley, A. C.; Steigerwald, M. L.; Nuckolls, C. *J Phys-Condens Mat,* **2008,** 20, (37).

(11) Dion, M.; Rydberg, H.; Schroder, E.; Langreth, D. C.; Lundqvist, B. I. *Phys. Rev. Lett.,* **2004,** 92, (24), 246401.
(12) Wellendorff, J.; Kelkkanen, A.; Mortensen, J. J.; Lundqvist, B. I.; Bligaard, T. *Top. Catal.,* **2010,** 53, (5-6), 378-383.
(13) Syomin, D.; Kim, J.; Koel, B. E.; Ellison, G. B. *J. Phys. Chem. B,* **2001,** 105, (35), 8387-8394.
(14) Lei, R. Z.; Gellman, A. J.; Koel, B. E. *Surf. Sci.,* **2004,** 554, (2-3), 125-140.
(15) Frei, M.; Aradhya, S. V.; Koentopp, M.; Hybertsen, M. S.; Venkataraman, L. *Nano Lett.,* **2011,** 11, (4), 1518-23.